Journal of Materials Chemistry C

Structural and luminescence properties of Nd3+/ Yb3+ codoped Al4B2O9 nanocrystalline powders

Journal:	*Journal of Materials Chemistry C*
Manuscript ID	TC-ART-06-2015-001696.R1
Article Type:	Paper
Date Submitted by the Author:	07-Oct-2015
Complete List of Authors:	Maia, Lauro; Universidade Federal de Goiás, Instituto de Física Faria Filho, Fausto; Universidade Federal de Goiás, Instituto de Física Jerez, Vladimir; Universidad de Investigación y Desarrollo, Grupo de Investigación FIELDS Moura, André; Universidade Federal de Alagoas, Grupo de Física da Matéria Condensada, Núcleo de Ciências Exatas, Campus de Arapiraca de Araújo, Cid; Universidade Federal de Pernambuco, Departamento de Física

Structural and luminescence properties of Nd^{3+}/Yb^{3+} codoped $Al_4B_2O_9$ nanocrystalline powders

Lauro J.Q. Maia [a,], Fausto M. Faria Filho [a], Vladimir Jerez [b,c], André L. Moura [c,d], and Cid B. de Araújo [c]*

[a,*] Grupo Física de Materiais, Instituto de Física, Universidade Federal de Goiás, Goiânia - GO, Brazil

[b] Grupo de Investigación FIELDS, Universidad de Investigación y Desarrollo, Bucaramanga, Colombia

[c] Departamento de Física, Universidade Federal de Pernambuco, 50670-901 Recife - PE, Brazil

[d] Grupo de Física da Matéria Condensada, Núcleo de Ciências Exatas, Universidade Federal de Alagoas, Campus de Arapiraca, Arapiraca - AL, Brazil

* Corresponding author: lauro@ufg.br

Abstract

Morphological, structural and optical properties of Nd^{3+}/Yb^{3+} codoped $Al_4B_2O_9$ nanopowders prepared by the polymeric precursor method were investigated. The compounds previously heat-treated at 900°C were characterized by X-ray diffraction (XRD) and high resolution transmission electron microscopy (HRTEM) techniques. The $Al_4B_2O_9$ nanocrystals obtained possess orthorhombic structure with grain dimensions between 10 and 20 nm. Photoluminescence (PL) spectra under excitation at 804 nm were collected and analyzed. The results indicate that the energy absorbed by the Nd^{3+} (transition: $^4I_{9/2} \rightarrow {}^4F_{5/2}+{}^2H_{9/2}$) is efficiently transferred to the Yb^{3+} in samples having 2 mol% of Nd^{3+} and 1 mol% of Yb^{3+}, increasing the emission from 930 nm to 1130 nm by 12.2 times in comparison with the samples doped with 1 mol% of Nd^{3+} and 1 mol% of Yb^{3+}. The dynamics of the PL process was also investigated. The PL decay at 975 nm from Yb^{3+} ($^2F_{5/2} \rightarrow {}^2F_{7/2}$) and at 1080 nm from Nd^{3+} ($^4F_{3/2} \rightarrow {}^4I_{11/2}$) was studied. The Yb^{3+} $^2F_{5/2}$ level lifetime varies from 201 to 48 μs while the lifetime of Nd^{3+} $^4F_{3/2}$ level varies from 121 to 69 μs when the Nd^{3+} concentration is changed from 1 to 8 mol%. On the other hand, the Yb^{3+} $^2F_{5/2}$ lifetime varies from 176 to 15 μs and the Nd^{3+} $^4F_{3/2}$ lifetime varies from 97 to 44 μs when the Yb^{3+} concentration is changed from 1 to 8 mol%, due to interactions between the rare-earth ions. The present results show that Nd^{3+}/Yb^{3+} codoped $Al_4B_2O_9$ nanocrystalline powders have large potential to be tested in solar energy concentrator and IR laser devices.

Keywords: aluminum borate phase; Nd^{3+}/Yb^{3+} transfer; efficient Yb^{3+} emission; structural and optical properties.

1 Introduction

Rare-earth (RE) trivalent ions can emit light at characteristic wavelengths due to intra-4f or internal 4f–5d transitions. These emissions occur from the near-infrared (NIR) to the ultraviolet (UV) and have been exploited for operation of devices such as waveguides, optical fiber amplifiers, solid state lasers, optical memories, solar cells, and displays. For instance, systems operating at ≈1μm, based on the ytterbium ions (Yb^{3+}) emission sensitized by neodymium ions (Nd^{3+}) are receiving much attention because of their potential applications in solar energy concentrators and high energy lasers.[1-5]

Multiple absorption bands of Nd^{3+} in the UV-NIR region can enhance the absorption of the solar light providing a variety of pumping options for Yb^{3+} to emit around 978 nm, which lies just above the band gap of Si (~1.1 eV) [1]. On the other hand, the high broadband emission of Yb^{3+} opens up greater opportunity for ultra-short pulsed lasers for thermonuclear fusion reactions [2]. Also laser action in the infrared from Yb^{3+} shows several interesting properties when compared to the more popular Nd^{3+} based lasers, including the absence of excited-state absorption processes, the possibility of a tunability range in the infrared (IR), as well as of mode-locking operation.[3]

Some Nd^{3+}/Yb^{3+} codoped materials have been synthesized and the energy transfer among the two ions was evaluated. Rakov and Maciel [4] studied the fluorescence of Yb^{3+} produced by efficient energy transfer from Nd^{3+} as a temperature sensor using yttrium silicate (Y_2SiO_5) crystalline powders prepared by combustion reaction. Lupei et al [5] investigated the $Nd^{3+}\rightarrow Yb^{3+}$ energy transfer characteristics in Y_2O_3 transparent ceramics, and the static spectral data revealed that the $Nd^{3+}\rightarrow Yb^{3+}$ energy transfer shows strong dependence on the Yb^{3+} content (less on Nd^{3+}). Recently, Nd^{3+}/Yb^{3+} doped TiO_2 samples exhibited strong NIR photoluminescence (PL) peak centered at 978 nm, which reveals efficient energy transfer from Nd^{3+} to Yb^{3+} in that matrix[6]. $Gd_3Ga_5O_{12}$: Yb^{3+},Nd^{3+} monocrystals were grown by Czochralski method and a very efficient Nd^{3+} ($^4F_{3/2}$) → Yb^{3+} ($^2F_{5/2}$) energy transfer was found. Besides, Nd^{3+}, Yb^{3+}, Ho^{3+}-doped beta-$Na(Y_{1.5}Na_{0.5})F_6$ luminescent phosphors were synthesized. In these compounds, green and red emissions due to Ho^{3+} were observed under 808 and 980 nm diode

laser excitations; Nd^{3+} can enhance the emissions of Ho^{3+} under 808 nm excitation, while it quenches Ho^{3+} emissions under excitation at 980 nm [7]. Indeed, there are several works on Nd^{3+} and/or Yb^{3+} doped materials due to its great applicability in optical devices, especially in high power lasers or in solar energy concentrators [4, 8-12].

Although some borate (crystalline and amorphous) materials present large potential for the applications mentioned above, they were not much exploited. In general the borate materials are good candidates because they present large transparency window from NIR to UV and large RE ions solubility. It was observed that the mechanical and chemical stabilities as well as the RE solubility of borate materials increase by the addition of aluminum oxide [13-15].

Aluminum borates are notable ceramic materials with high elastic modulus, tensile strength, and low thermal expansion properties attractive for optoelectronic, structure applications, and tribology [16]. $Al_4B_2O_9$ have orthorhombic structure with cell parameters of *a* = 14.746 Å, *b* = 15.268 Å and *c* = 5.557 Å [17, 18] which have potential in oxidation-resistant reinforced composites, chemical and heat-insulating materials, and filter media [16]. This phase has been synthesized as nanowires, nanotubes, whiskers and their mechanical properties have been already studied.[19-22]

Li and Chang [19] in 2006 synthesized $Al_4B_2O_9$ by the CVD method using boron triiodide (BI_3) vapor with Ar gas as precursor at 750 - 850 ^oC, and thick Al films deposited on the polished sides of sapphire substrates were used as catalysts. In 2007, Elssfah *et al* [20] synthesized by direct calcination of a precursor powder made of $Na_2B_4O_7{\cdot}10H_2O$ and $Al(NO_3)_3{\cdot}9H_2O$ at 850 ^oC. Tao *et al* [21] synthesized by a one-step combustion method between 900 and 1050 ^oC, using $Al(NO_3)_3{\cdot}9H_2O$, H_3BO_3, NH_4NO_3, and $C_6H_8O_7{\cdot}H_2O$ previously dissolved in water. Wang and co-workers [22] synthesized by a route based on the calcination of amorphous aluminum borate, which was prepared by the precipitation reaction between aluminum isopropoxide and H_3BO_3 isopropyl alcohol solution. In these works, the authors only exploited the structural and mechanical properties of the $Al_4B_2O_9$ material. Recently, Zheng and Chen [23] synthesized Eu^{2+}-doped $Al_4B_2O_9$, via a modified solid-state reaction, using urea as an auxiliary reagent at 850 ^oC (a type of combustion reaction method), in which blue light emissions were studied

under ultraviolet excitations. For instance, only Zheng and Chen [23] have studied the $Al_4B_2O_9$ materials doped with RE ions, the Eu^{2+}. None of these works studied infrared emissions from Nd^{3+} and Yb^{3+} ions, neither used the polymeric precursor method to prepare the samples.

The main advantage of the polymeric precursor method (a soft chemistry route), when compared with the solid-state reaction, combustion reaction and co-precipitation methods, is the fact that the homogeneous distribution of chemical elements at the atomic scale on the solution is maintained until the end of the process when a powdered sample is obtained [24]. The polymeric precursor method is quite attractive for the preparation of multi-component systems since the use of different components at a molecular level can be easily achieved in solutions, not requiring controlled atmosphere. On the other hand, the main disadvantage of this method is the fact that the resin, from which the powder is obtained, contains a high amount of organic materials that is incorporated during the polymerization process. Thus, a thermal treatment between 400 ^oC and 700 ^oC, must be made to remove the organic constituents [13].

Based on these trends and physical characteristics, in this work we investigated the morphological, structural and optical properties of Nd^{3+}/Yb^{3+} codoped $Al_4B_2O_9$ nanopowders prepared by the polymeric precursor method. Photoluminescence (PL) emissions and the decay time of the Nd^{3+} transition $^4F_{3/2} \rightarrow {}^4I_{11/2}$ (emission at 1080 nm) and the Yb^{3+} transition $^2F_{5/2} \rightarrow {}^2F_{7/2}$ (emission at 975 nm) were measured. Finally, we analyzed the energy transfer between Nd^{3+} and Yb^{3+} varying the relative concentration of Nd^{3+} and Yb^{3+} and the best relation among these ions in this matrix was determined.

2 Experimental Section

2.1 Sample preparation

The materials' compositions selected for our experiments were xNd^{3+}/yYb^{3+} codoped $Al_4B_2O_9$, with x, y = 1, 0; 1, 1; 1, 2; 1, 4; 1, 8; 0, 1; 2, 1; 4, 1; and 8, 1 in mol%. Aluminum nitrate nonahydrate ($Al(NO_3)_3.9H_2O$, Vetec 98%), boric acid (H_3BO_3, Ecibra 99.5%), neodymium nitrate pentahydrate ($Nd(NO_3)_3.6H_2O$, Sigma-Aldrich 99.9%), and ytterbium nitrate pentahydrate ($Yb(NO_3)_3.5H_2O$, Sigma-

Aldrich 99.9%), were used in the polymeric precursor method. Citric acid anhydrous ($C_5O_7H_8$, Sigma-Aldrich 99.5%) and *d*-sorbitol ($C_6O_6H_{14}$, Sigma-Aldrich 98%) were used in this route as complexant and polymerization agents, respectively. The synthesis of the resin was achieved by dissolving aluminum, neodymium and ytterbium nitrates in an aqueous solution of citric acid at room temperature during 60 minutes, forming metallic citrates. This solution was added to another solution of *d*-sorbitol and boric acid dissolved previously in water during 30 minutes to produce boron complexes. This new solution maintained at 80 ^oC during 30 minutes under magnetic stirring (~600 rpm) to form a wet resin. The molar ratio of citric acid to elements (metals + boron) was 3:1. The citric acid/d-sorbitol mass ratio was set to 3:2. Sufficient water was added to dissolve all the precursors under stirring, approximately 300 ml of H_2O for 5 g of Nd^{3+}/Yb^{3+} codoped $Al_4B_2O_9$. The resins were dried at 150 ^oC during 5 hours and calcinated at 400 ^oC for 24 hours, respectively. Finally, the powders were heat-treated at 900 ^oC during 1 hour under atmospheric air.

2.2 Characterization

X-ray diffraction (XRD) measurements were taken with a Bruker D8 Discover diffractometer equipped with a copper tube operating at 40 kV and 40 mA and coupled to a *Johansson* monochromator for $K\alpha_1$. Bragg-Brentano theta-2 theta geometry with unidimensional *Lynxeye*® detector and step scan of 0.005^o with 1 second in each step were used. During the measurements, the samples were rotated at 15 rpm to minimize the preferential orientation. Corundum was used as external standard.

The samples were characterized by using a JEOL JEM 2010 high-resolution transmission electron microscopy (HRTEM) operating at 200 keV; selected area electron diffraction (SAED) patterns were also analyzed.

Infrared emission spectra recorded from 850 to 1400 nm were obtained using a monochromator and an InGaAs photodiode as detector (Fluorolog FL3-221 from Horiba Jobin-Yvon), under excitation at 804 nm from a CW laser diode delivering 150 mW.

PL from the Yb^{3+} at 975 and Nd^{3+} at 1080 nm were measured using an optical parametric oscillator (OPO), operating at 804 nm, pumped by the second harmonic from a Nd:YAG laser (7 ns, 5 Hz). The OPO beam was focused on the sample using a 10 cm focal length lens. The signal emitted by the sample was collected using a 10 cm focal length lens along 45° direction with respect to the laser beam propagation direction. The PL signal was selected by a monochromator with 0.2 nm of resolution and detected by a photodetector with nanosecond response, coupled to a computer and connected to a digital oscilloscope (with 100 MHz bandwidth). Two RG850 filters were used to reject the scattered excitation light. For the optical measurements the powder sample was gently pressed inside metallic holders (5 mm diameter, 2 mm height). All measurements were made at room temperature.

3 Results and discussion

Figures 1(a) and (b) shows XRD patterns obtained from a powder heat-treated at 900 ^{o}C during 1 hour. The $Al_4B_2O_9$ crystalline phase was clearly detected but no diffraction peaks associated to Nd_2O_3 or Yb_2O_3 were observed for all RE concentrations used. The results indicate that the RE ions can be located inside the crystallites, and probably also on the particles' surface. The diffraction lines positions from the JCPDS card number 29-0010 [18] are included in Figures 1(a) and 1(b) for comparison with the samples' data. The $Al_4B_2O_9$ structure is orthorhombic and presents the Pbam (55) space group, with cell parameters *a* = 14.746 Å, *b* = 15.268 Å, and *c* = 5.557 Å.[18]

Figure 1

Analyzing the main peak position at ~16.6^{o}, a shift to lower angles by increasing the Yb^{3+} or Nd^{3+} contents was observed. This behavior indicates that Nd^{3+} or Yb^{3+} replaces Al^{3+} ions of $Al_4B_2O_9$ crystalline structure.

The average crystallite size was determined from the full-width at half maximum (FWHM) of the main XRD peak (Figures 1(a) and 1(b)) (See also Figures S1(a) and S1(b) of the Supplementary Information) and using the Scherrer equation:[25, 26]

$$D_{hkl} = \lambda k / \beta \cos\theta , \quad (1)$$

where λ is the Cu $K\alpha$ wavelength, θ is the diffraction angle, k is a constant equal to 0.9 for spherical particles, and β is the half-width of the diffraction peak. The β-value was determined based on the equation:

$$\beta = (B_{obs}^2 - b^2)^{1/2}, \quad (2)$$

where B_{obs} is the FWHM of the sample and b is the FWHM of an external standard (corundum).

The variation of the crystallite size as a function of the Yb^{3+} and Nd^{3+} concentrations is shown in Figure 1(c). The sizes, determined based on the (220) crystal plane of $Al_4B_2O_9$ centered at ≈16.6°, vary from 15.8 to 8.5 nm by increasing the Yb^{3+} concentration, and from 16.0 to 8.7 nm by increasing the Nd^{3+} concentration. These results suggest that the RE ions act as limiters for growth of $Al_4B_2O_9$ nanocrystallites, and almost the same effect was observed for samples with 4 and 8%, probably due to the RE solubility limit in the $Al_4B_2O_9$ phase.

Few papers in the literature report on the synthesis and structural properties of the $Al_4B_2O_9$ orthorhombic structure [16, 19, 21-23]. Zhang et al [16] demonstrated the production of single-crystals of $Al_4B_2O_9$ nanorods via simple thermal chemical route at 1050 °C under air atmosphere. The nanorods had uniform diameters from 30 to 50 nm and lengths higher than 1000 nm. Li and Chang [19] obtained single crystals of $Al_4B_2O_9$ as nanowires and nanotubes on sapphire substrates covered by an aluminum film, using the chemical vapor deposition method between 750 – 850 °C, and all nanostructures have diameters from 10 to 500 nm and lengths from 300 to 2000 nm. Tao et al [21] used one-step combustion method to synthesize $Al_4B_2O_9$ nanowires and propose their uses for designing nanocomposites and nanodevices due to its high hardness and elastic modulus. Whiskers of $Al_4B_2O_9$ with diameters around 400 nm and lengths from 3000 to 5000 nm were obtained by Wang et al [22] from an amorphous precursor. Only Zheng and Chen [23] produced Eu^{2+} doped $Al_4B_2O_9$ nanoparticles

containing with 20 – 50 nm in diameter by the solid state reaction at 850 ^{o}C to be used as phosphors. To the best of our knowledge, there is no report on the Nd^{3+} and/or Yb^{3+} doping $Al_4B_2O_9$ phase.

Based on the peak position from XRD data in Figures 1(a) and 1(b), the Miller index of the diffracted planes in JCPDS card number 29-0010, and using the Rede 93 software program developed by Paiva Santos et al [27], the *a*, *b*, and *c* cell parameters of the $Al_4B_2O_9$ host as a function of the Nd^{3+} and/or Yb^{3+} concentration were calculated and shown in Figure 1(d). We observed an increase of the cell parameters by adding and increasing the Nd^{3+} or Yb^{3+}, as a clear demonstration that these ions were incorporated into the matrix**;** for 8% mol of Nd^{3+} or Yb^{3+} the increase is similar to 4 mol%. These behaviors can be well correlated to the crystallite size changes in Figure 1(c). Also, the cell parameters ratios change, as can be seen in Figure S1(c) of the Supplementary Information. The error bars of the cell parameter are due to the nanometric size of the crystallites, crystallinity degree of the samples and are associated to the large FWHM of the diffraction peaks. Especially for the high RE ions concentrations, a fraction of ions did not incorporate to the nanocrystals being located on the crystallite surfaces; as a consequence, it is expected that its photoluminescence will be influenced by defects, hydroxyl groups and atmospheric air moisture.

Boron does not present ionic character and into the crystalline matrix form groups, like: BO_3 and/or BO_4. On the other hand aluminum elements in crystals normally have an ionic character. The radius of boron and aluminum are 0.23 Å and 0.54 Å, respectively, while, Nd^{3+} and Yb^{3+} possess ionic character having radius of 1.12 Å and 0.99 Å, respectively [28]. It is known that aluminum in crystals is coordinated by 6 oxygen atoms, and the RE ions present coordination from 6 to 9 depending on the matrix and synthesis procedure. Therefore we suggest that Nd^{3+} and Yb^{3+} replace Al^{3+} ions into the $Al_4B_2O_9$ crystalline structure.

Figure 2 shows HRTEM images and SAED patterns of the crystallized samples at 900 ºC containing $1Nd^{3+}/2Yb^{3+}$ (Figures 2(a), 2(b), 2(c) and 2(d)) and $2Nd^{3+}/1Yb^{3+}$ (Figures 2(e), 2(f), 2(g) and 2(h)). Note that the $Al_4B_2O_9$ crystallites possess well defined structural planes composed of almost spherical shape with size ranging from 10 to 20 nm. In the case of Figures 2(c) and 2(g) the

nanoparticles present high crystallinity with diameters of 16 and 18 nm, respectively (For additional results see Figure S2 of the Supplementary Information). In both samples, the same distance of 0.52 nm between the planes was measured, corresponding to the (220) plane of $Al_4B_2O_9$ (according to the JCPDS # 29-0010 card [18]).

Note that the nanoparticles measured by HRTEM form agglomerates of sizes between 100 - 150 nm and the SAED patterns were the same for both samples showing polycrystalline agglomerates. The crystallite sizes measured by HRTEM have dimensions of the same order of magnitude as determined by XRD patterns.

Figure 2

The SAED patterns for both samples (images 2d and 2h) show concentric and narrow circles. Bright points onto circles were observed. These features indicate that the nanocrystallites agglomerated as 100 – 150 nm particles that contain some $Al_4B_2O_9$ single crystals randomly oriented as well as a certain number with a preferential orientation.

To characterize the PL properties of the nanocrystals, the samples were excited at 804 nm, and the PL spectra were recorded from 850 nm (11765 cm^{-1}) to 1400 nm (7143 cm^{-1}). Figure 3(a) illustrates the normalized spectra as a function of the Yb^{3+} concentration for a fixed Nd^{3+} concentration, and Figure 3(b) shows the normalized spectra as a function of the Nd^{3+} concentration for a fixed Yb^{3+} concentration. All spectra were normalized by its maximum intensity. To calculate the emission intensity from the samples, the collected spectra (before the normalizing procedure, shown in the Figure S3 of the Supplementary Information) had the wavelengths (in nm) converted in wavenumber (cm^{-1}) that is directly proportional to energy spectra and then the emission curves were integrated from 930 nm (10753 cm^{-1}) to 1130 nm (8850 cm^{-1}). In the sample containing $1Nd^{3+}/0Yb^{3+}$ it was observed Nd^{3+} emissions due to the $^4F_{3/2} \rightarrow {}^4I_{9/2}$, $^4F_{3/2} \rightarrow {}^4I_{11/2}$, and $^4F_{3/2} \rightarrow {}^4I_{13/2}$ transitions, centered at ~900 nm (11111 cm^{-1}), ~1060 nm (9434 cm^{-1}) and ~1330 nm (7519 cm^{-1}), respectively. For the codoped

samples: $1Nd^{3+}/1Yb^{3+}$, $1Nd^{3+}/2Yb^{3+}$, $1Nd^{3+}/4Yb^{3+}$, $1Nd^{3+}/8Yb^{3+}$, $2Nd^{3+}/1Yb^{3+}$, $4Nd^{3+}/1Yb^{3+}$, and $8Nd^{3+}/1Yb^{3+}$, only emissions between 930 and 1130 nm were observed due to the $^2F_{5/2} \rightarrow {}^2F_{7/2}$ transition of Yb^{3+} with maximum emissions around 975 nm (10256 cm^{-1}) and 1012 nm (9881 cm^{-1}), and the $^4F_{3/2} \rightarrow {}^4I_{11/2}$ transition of Nd^{3+} with maximum emission around 1060 nm (9434 cm^{-1}). The integrated intensities as a function of Nd^{3+} or Yb^{3+} concentrations are shown in Figure 3(c). The relative integrated intensities can be compared because all spectra were collected with samples having the same mass and placed in the same position with respect to the excitation beam and detector position; we recall that all samples contained grains with approximately the same size distribution. Increasing the Yb^{3+} concentration, stronger emission was observed for the sample with relative concentration $1Nd^{3+}/2Yb^{3+}$ that indicates the largest energy transfer from Nd^{3+} to Yb^{3+}. This was already observed for other crystalline hosts but the authors evaluated changes with respect to the Yb^{3+} content, with a fixed concentration of Nd^{3+} [1, 4, 5]. Here we also evaluated the PL spectra increasing the concentration of Nd^{3+} for a fixed Yb^{3+} concentration, and the best relation between the Nd^{3+} and Yb^{3+} concentrations was determined. The PL emission relation between $2Nd^{3+}/1Yb^{3+}$ and $1Nd^{3+}/2Yb^{3+}$ samples is 7.8. Surprisingly, the best result occurs for $2Nd^{3+}/1Yb^{3+}$ with 12.2 times higher than that for $1Nd^{3+}/1Yb^{3+}$. Since the Nd^{3+} ions are directly excited by the laser at 804 nm, its higher concentration favors the growth of the energy transfer rate to the Yb^{3+} and maybe protect the emitting ions from structural defects and hydroxyl or carbonyl group residues, that could reduce the Nd^{3+} emission. Also, as will be discussed latter, the Yb^{3+} can favor the Nd^{3+} to have a more homogeneous distribution inside the samples reducing the Nd^{3+}-Nd^{3+} pair interactions, and favoring the energy migration from Nd^{3+} to Yb^{3+}. All these effects may contribute to the higher PL efficiency observed for the $2Nd^{3+}/1Yb^{3+}$ codoped samples.

Figure 3

To evaluate the emission centers in more details and the energy transfer processes between the active ions, like Nd^{3+}-Nd^{3+}, Nd^{3+}-Yb^{3+}, and Yb^{3+}-Yb^{3+} pairs, the PL decay at 975 nm (10256 cm^{-1}) and 1080 nm (9259 cm^{-1}) were measured for Yb^{3+} ($^2F_{5/2} \rightarrow {}^2F_{7/2}$) transition and Nd^{3+} ($^4F_{3/2} \rightarrow {}^4I_{11/2}$) transition, respectively, under excitation at 804 nm (12438 cm^{-1}) with the pulsed OPO. As can be seen in Figure 3(a), for the Nd^{3+}/Yb^{3+} codoped $Al_4B_2O_9$ the band centered in 1060 nm is mainly due to Nd^{3+} from the $^4F_{3/2} \rightarrow {}^4I_{9/2}$ transition, but the emissions centered at 975 and 1012 nm are due to Yb^{3+}. Then, to measure the Nd^{3+} $^4F_{3/2}$ level lifetime we collected the emission at 1080 nm because Yb^{3+} does not emit in this region.

The decay kinetics of Yb^{3+} and Nd^{3+} can be used to determine important parameters of the $Nd^{3+} \rightarrow Yb^{3+}$ energy transfer such as the nature of the Nd^{3+}-Yb^{3+} coupling and the energy-transfer microparameter. Furthermore, lifetime measurements are also used to evaluate the radiative or nonradiative mechanism of the $Nd^{3+} \rightarrow Yb^{3+}$ energy transfer.

Figures 4(a) and 4(b) illustrate the PL decay curves as a function of the Yb^{3+} concentration at 1080 and 975 nm, respectively, while Figures 4(c) and 4(d) show the PL behavior as a function of the Nd^{3+} concentration.

Figure 4

Figure 5

Notice that most of the samples do not exhibit single exponential decay that is probably related to the Nd^{3+}-Yb^{3+} coupling and quenching effect due to energy transfer between Nd^{3+} ions. For all samples, the average lifetime, τ, was calculated by:

$$\tau = \int_{t_0}^{t_f} \frac{I(t)}{I_0} dt \qquad (3)$$

where *I(t)* is the PL intensity at time *t*, I_0 is the PL intensity at $t = t_0$ that corresponds to 0 μs while t_f is the time at which the PL intensity becomes zero (~1000 μs). Figures 5(a) and 5(b) show the decay time behavior for emissions at 975 and 1080 nm as a function of the Nd^{3+} and Yb^{3+} concentration, respectively.

Changing the Nd^{3+} concentration, the decay time of the Nd^{3+} transition ($^4F_{3/2} \rightarrow {}^4I_{11/2}$) at 1080 nm increased reaching a maximum of ~120 μs in the interval from 1 to 4 mol%; however a large reduction is observed for 8 mol% of Nd^{3+}. In spite of it, the emission at 975 nm, corresponding to the $^2F_{5/2} \rightarrow {}^2F_{7/2}$ transition of Yb^{3+}, presents maximum decay time of ~200 μs for the sample with 2 mol% of Nd^{3+}. This is a strong indication that the interaction Yb^{3+} - Nd^{3+} ions is relevant even for low concentration of Nd^{3+}. At high Nd^{3+} concentrations, the Nd^{3+}-Nd^{3+} interaction are well pronounced contributing to reduce significantly the Nd^{3+} and Yb^{3+} decay times and their emission intensities (Figure 3(c)).

These results suggest that a large fraction of the Yb^{3+} ions are coupled to Nd^{3+} ions, favoring the energy transfer process from the excited Nd^{3+} ions to the Yb^{3+} ions in the ground state. Analyzing the PL intensity dependence with the Yb^{3+} concentration, a similar behavior was observed for the emission at 1080 nm (transition $^4F_{3/2} \rightarrow {}^4I_{11/2}$ of Nd^{3+}) with maximum between 1 and 2 mol% and decay time of ~100 μs. The largest decay time of the emission at 975 nm was ~175 μs for the sample with 1 mol% of Yb^{3+}. Indeed while increasing the Yb^{3+} concentration it is observed that the decay time decreases exponentially. We recall that similar results related to the energy transfer from Nd^{3+} to Yb^{3+} ions were observed by Jaque et al [3] for Nd^{3+} doped $YAl_3(BO_3)_4$. The same behavior was reported by Garskaite et al [6] for Nd^{3+}/Yb^{3+} doped TiO_2 materials. Lupei et al [2, 5] observed that $Nd^{3+} \rightarrow Yb^{3+}$ energy transfer in Y_2O_3 transparent ceramics show a strong dependence on the Yb^{3+} content but smaller for the Nd^{3+} content variation.

Jaque et al [3] have calculated the energy transfer efficiency (η_t) in Nd^{3+}/Yb^{3+} codoped $YAl_3(BO_3)_4$ monocrystals from time decay experiments by

$$\eta_t = 1 - \frac{\tau_{Nd-Yb}}{\tau_{Nd}} \quad (4)$$

where τ_{Nd} and $\tau_{Nd\text{-}Yb}$ are the Nd^{3+} $^4F_{3/2}$ PL lifetime obtained for Nd^{3+} and Nd^{3+}/Yb^{3+} codoped samples with the same Nd^{3+} concentration. They observed an increase of η_t from 0.40 to 0.62 for Yb^{3+} concentration in the 0.2 – 10 at.% range. Using equation (4) to calculate η_t for our $1Nd^{3+}/yYb^{3+}$ codoped $Al_4B_2O_9$, with y = 0; 1; 2; 4; 8 samples, the following values were determined: 0, -0.39, -0.37, 0.13 and 0.37, respectively. This result lead us to conclude that changing the Yb^{3+} concentration with a fixed Nd^{3+} concentration of 1mol% in $Al_4B_2O_9$ can increase the dispersion of Nd^{3+} ions. The explanation for the negative values of the $1Nd^{3+}/1Yb^{3+}$, $1Nd^{3+}/2Yb^{3+}$ codoped samples is due to the coexistence of the following two effects: one is Yb^{3+} favor Nd^{3+} to have a better distribution in the samples reducing the Nd^{3+}-Nd^{3+} pairs interactions, increasing the Nd^{3+} $^4F_{3/2}$ lifetime when compared to that for single doped Nd^{3+} sample; and the other effect is related to an energy migration competition from Nd^{3+} to Yb^{3+}. Note that Nd^{3+} $^4F_{3/2}$ lifetime of $1Nd^{3+}/1Yb^{3+}$ and $1Nd^{3+}/2Yb^{3+}$ codoped samples are almost equal (Figure 5(b)), but the emission intensity of $1Nd^{3+}/2Yb^{3+}$ sample is 57% higher than that of $1Nd^{3+}/1Yb^{3+}$ sample. On the other hand, in samples with $1Nd^{3+}/4Yb^{3+}$ and $1Nd^{3+}/8Yb^{3+}$ concentrations, the Nd^{3+} are strongly coupled with Yb^{3+} and η_t change from 0.13 to 0.37; the Yb^{3+}-Yb^{3+} pairs are also formed and energy migration between Yb^{3+} ions occurs and energy suppression take place leading to a low PL intensity. It was not possible to measure the $^2F_{5/2}$ lifetime of single doped Yb^{3+} sample because no PL was observed under excitation at 804 nm with the pulsed OPO. Then, the η_t values and the changes by increasing the Nd^{3+} concentration could not be calculated.

Finally, it was observed in curves presented in Figures 4(a) – (d) a reduction of rise-time by increasing Nd^{3+} and/or Yb^{3+} concentrations. These effects are related to the Nd^{3+}-Yb^{3+}, Yb^{3+}-Yb^{3+}, and Nd^{3+}-Nd^{3+} ions interactions. The absorption transient time was not determined because the sample with higher RE concentrations present rise-times faster than our detector response.

4 Conclusion

In summary, $Al_4B_2O_9$ nanocrystals codoped with Nd^{3+} and Yb^{3+} were prepared by a chemical route and successfully studied for their structural, microstructural, luminescence and energy transfer properties. Only single orthorhombic $Al_4B_2O_9$ phase was observed and the structural details were well-matched with the JCPDS Card # 29-0010. Increasing the Yb^{3+} or Nd^{3+} concentration from 0 mol% to 4 mol%, the $Al_4B_2O_9$ crystallite sizes decrease from ~16 nm to ~9 nm, which is related to those observed by HRTEM images. The Yb^{3+} concentration of 2 mol% was found to be an optimum choice for sensitized Yb^{3+} luminescence. An efficient $Nd^{3+} \rightarrow Yb^{3+}$ energy transfer was observed and the best relative concentration $[Nd^{3+}]/[Yb^{3+}]$ was 1/2. The energy transfer pathway is initiated by absorption of the incident light by the Nd^{3+} that act as donors to the acceptors and Yb^{3+} emitters. The decay times of the Nd^{3+} transition $^4F_{3/2} \rightarrow {}^4I_{11/2}$ (emission at 1080 nm) and the Yb^{3+} transition $^2F_{5/2} \rightarrow {}^2F_{7/2}$ (emission at 975 nm) are influenced by the relative concentration of the rare-earth ions. The decay time of the emission at 1080 nm (975 nm) as a function of the Nd^{3+} concentration, presented a maximum value of ~120 μs for 4 mol% (~200 μs for 2 mol%). Changing the Yb^{3+} concentration, the maximum decay time measured at 1080 nm (975 nm) was ~100 μs (175 μs) for 1 mol% of Yb^{3+}. The results obtained show that Nd^{3+}/Yb^{3+} codoped $Al_4B_2O_9$ nanocrystals are a good candidate to be tested in solar energy concentrators and high power infrared lasers.

Acknowledgements

The work was performed in the frameworks of the National Institute of Photonics (INCT de Fotônica), PRONEX-CNPq/FACEPE, UNIVERSAL-FAPEG, UNIVERSAL-CNPq, CT-ENERG/CNPq and CASADINHO/PROCAD-CNPq/CAPES projects. André L. Moura and Vladimir Jerez acknowledge the CNPq for their postdoctoral fellowships. Vladimir Jerez also acknowledges the Universidad de Santander-UDES and COLCIENCIAS from Colombia.

References

[1] A. D. Sontakke, K. Biswas, R. Sen and K. Annapurna, *J. Opt. Soc. Am. B*, **2012**, *27*, 2750.

[2] A. Lupei, V. Lupei, A. Ikesue and C. Gheorghe, *J. Opt. Soc. Am. B*, 2010, *27*, 1002.

[3] D. Jaque, M. O. Ramirez, L. E. Bausa, J. Garcia Sole, E. Cavalli, A. Speghini and M. Bettinelli, *Phys. Rev. B*, **2003**, *68*, 035118.

[4] N. Rakov and G. S. Maciel, *Opt. Lett.*, **2014**, *39*, 3767.

[5] A. Lupei, V. Lupei, A. Ikesue, C. Gheorghe and S. Hau, *Opt. Mater.*, **2010**, *32*, 1333.

[6] E. Garskaite, A. S. Flø, A. T. J. van Helvoort, A. Kareiva and E. Olsen, *J. Lumin.*, **2013**, *140*, 57.

[7] X. Wang, S. Xiao, Y. Bu and J. W. Ding, *J. Alloys Comp.*, **2009**, *477*, 941.

[8] N. Sugimoto, Y. Ohishi, Y. Katoh, A. Tate, M. Shimokozono, S. Sudo, *Appl. Phys. Lett.*, **1995**, *67*, 582.

[9] A. Majchrowski, S. Klosowicz, L. R. Jaroszewicz, M. Swirkowicz, I. V. Kityk, M. Piasecki and M. G. Brik, *J. Alloys Comp.*, **2010**, *491*, 26.

[10] Z. Jia, A. Arcangeli, X. Tao, J. Zhang, C. Dong, M. Jiang, L. Bonelli and M. Tonelli, *J. Appl. Phys.*, **2009**, *105*, 083113.

[11] P. Dekker and J. M. Dawes, *Opt. Express*, **2004**, *12*, 5922.

[12] R. Reisfeld and Y. Kalisky, *Chem. Phys. Lett.*, **1981**, *80*, 178.

[13] L. J. Q. Maia, A. Ibanez, L. Ortega, V. R. Mastelaro and A. C. Hernandes, *J. Nanopart. Res.*, **2008**, *10*, 1251.

[14] L. J. Q. Maia, V. R. Mastelaro, A. C. Hernandes, J. Fick and A. Ibanez, *Thin Solid Films*, **2009**, *517*, 6584.

[15] N. Hemono, J. Rocherulle, M. Le Floch, B. Bureau and P. Benard-Rocherulle, *J. Mater. Sci.*, **2006**, *41*, 445.

[16] J. Zhang, J. Lin, H.S. Song, E.M. Elssfah, S.J. Liu, J.J. Luo, X.X. Ding, C. Tang and S.R. Qi, *Mater. Lett.*, **2006**, *60*, 3292.

[17] Joint Committee for Powder Diffraction Standards, JCPDS Powder Diffraction File, File Card No. 09-0158, **1998**.

[18] Joint Committee for Powder Diffraction Standards, JCPDS Powder Diffraction File, File Card No. 29-0010, **1998**.

[19] Y. Li and R. P. H. Chang, *Mater. Chem. Phys.*, **2006**, *97*, 23.

[20] E. M. Elssfah, C. C. Tang, J. Zhang, H. S. Song, X. X. Ding and S. R. Qi, *Mater. Res. Bull.*, **2007**, *42*, 482.

[21] X. Tao, X. Wang and X. Li, *Nano Lett.*, **2007**, *7*, 3172.

[22] J. Wang, G. Ning, X. Yang, Z. Gan, H. Liu and Y. Lin, *Mater. Lett.*, **2008**, *62*, 1208.

[23] Y. Zheng and D. Chen, *J. Lumin.*, **2011**, *26*, 481.

[24] L. J. Q. Maia, C. R. Ferrari, V. R. Mastelaro, A. C. Hernandes, A. Ibanez, *Solid State Sciences*, **2008**, *10*, 1835.

[25] H. P. Klug and L. E. Alexander, *X-Ray Diffraction Procedures for Polycrystalline and Amorphous Materials*, Wiley: New York, **1954**.

[26] L. J. Q. Maia, M. I. B. Bernardi, A. R. Zanatta, A. C. Hernandes and V. R. Mastelaro, *Mater. Sci. and Eng. B*, **2004**, *107*, 33.

[27] C. O. Paiva Santos, D. Garcia, Y. P. Mascarenhas, J. A. Eiras, Cerâmica, **1989**, *35*, 153.

[28] W. M. Haynes, *Handbook of Chemistry and Physics*, 95th ed., CRC Press: Boca Raton, **2014**.

Figure captions

Figure 1: X-ray diffraction pattern of $Al_4B_2O_9$ powders heat-treated at 900 ^oC increasing the concentration of (a) Yb^{3+} ions; (b) Nd^{3+} ions. The diffraction pattern of the JCPDS card number 29-0010 is also shown for reference. (c) Crystallite size and (d) cell parameters of $Al_4B_2O_9$ phase synthesized at 900 ^oC as a function of Yb^{3+} or Nd^{3+} ions concentration.

Figure 2: HRTEM images and SAED spectra of $Al_4B_2O_9$ nanopowders heat-treated at 900 ^oC for $1Nd^{3+}/2Yb^{3+}$ (a), (b), (c) and (d), and for $2Nd^{3+}/1Yb^{3+}$ (e), (f), (g) and (h).

Figure 3: Normalized photoluminescence (PL) spectra of $Al_4B_2O_9$ powders heat-treated at 900 ^oC: (a) with 1 Nd^{3+} mol% and changing the Yb^{3+} concentration; (b) with 1 Yb^{3+} mol% and changing the Nd^{3+} concentration. All spectra were measured at room temperature under excitation at 804 nm. (c) Integrated PL intensity as a function of Yb^{3+} and Nd^{3+} concentration between 930 and 1130 nm.

Figure 4: Photoluminescence decay signal corresponding to: the $^2F_{5/2} \rightarrow {}^2F_{7/2}$ transition of Yb^{3+} (emission at 975 nm) and the $^4F_{3/2} \rightarrow {}^4I_{11/2}$ transition of Nd^{3+} (emission at 1080 nm) as a function of Yb^{3+} concentration (a and b); the emission at 975 nm and the emission at 1080 nm as a function of Nd^{3+} concentration (c and d)..

Figure 5: Decay time behavior of the emissions at 975 nm and at 1080 nm with (a) Yb^{3+} and (b) Nd^{3+} doping concentration for $Al_4B_2O_9$.

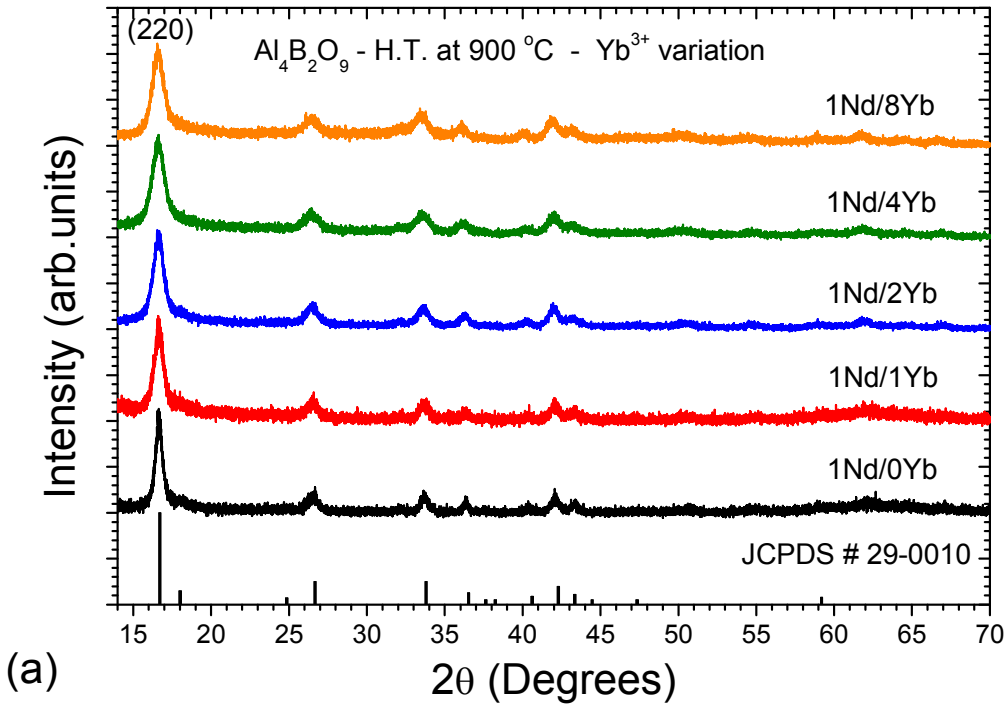
(220)
$Al_4B_2O_9$ - H.T. at 900 °C - Yb^{3+} variation
1Nd/8Yb
1Nd/4Yb
1Nd/2Yb
1Nd/1Yb
1Nd/0Yb
JCPDS # 29-0010
Intensity (arb.units)
15 20 25 30 35 40 45 50 55 60 65 70
2θ (Degrees)

(a)

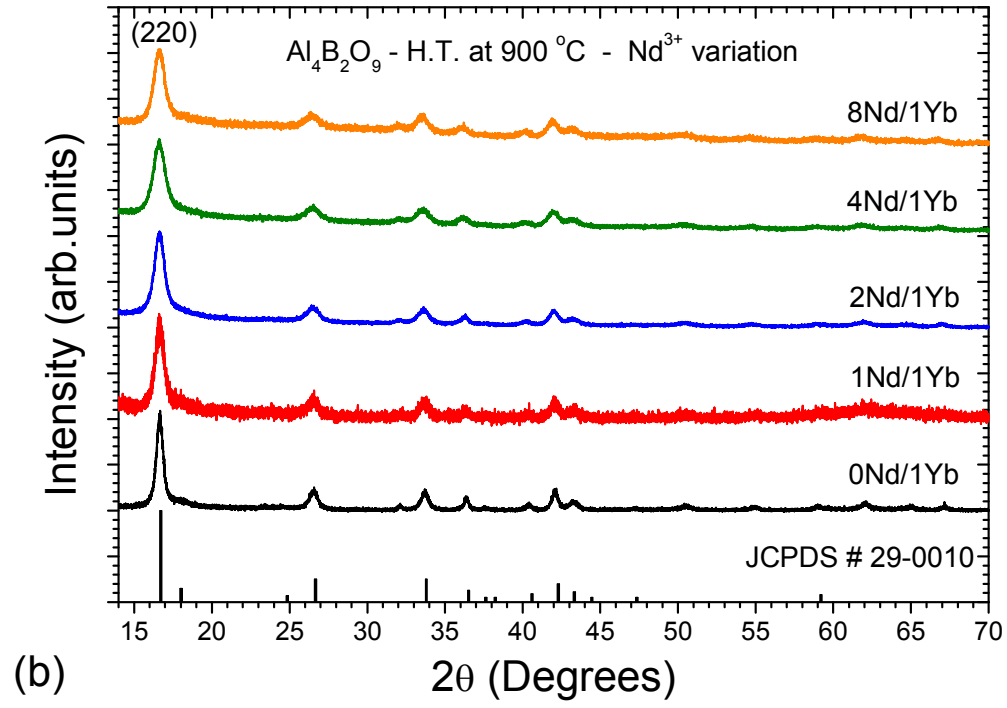
(220)
$Al_4B_2O_9$ - H.T. at 900 °C - Nd^{3+} variation
8Nd/1Yb
4Nd/1Yb
2Nd/1Yb
1Nd/1Yb
0Nd/1Yb
JCPDS # 29-0010
Intensity (arb.units)
15 20 25 30 35 40 45 50 55 60 65 70
2θ (Degrees)

(b)

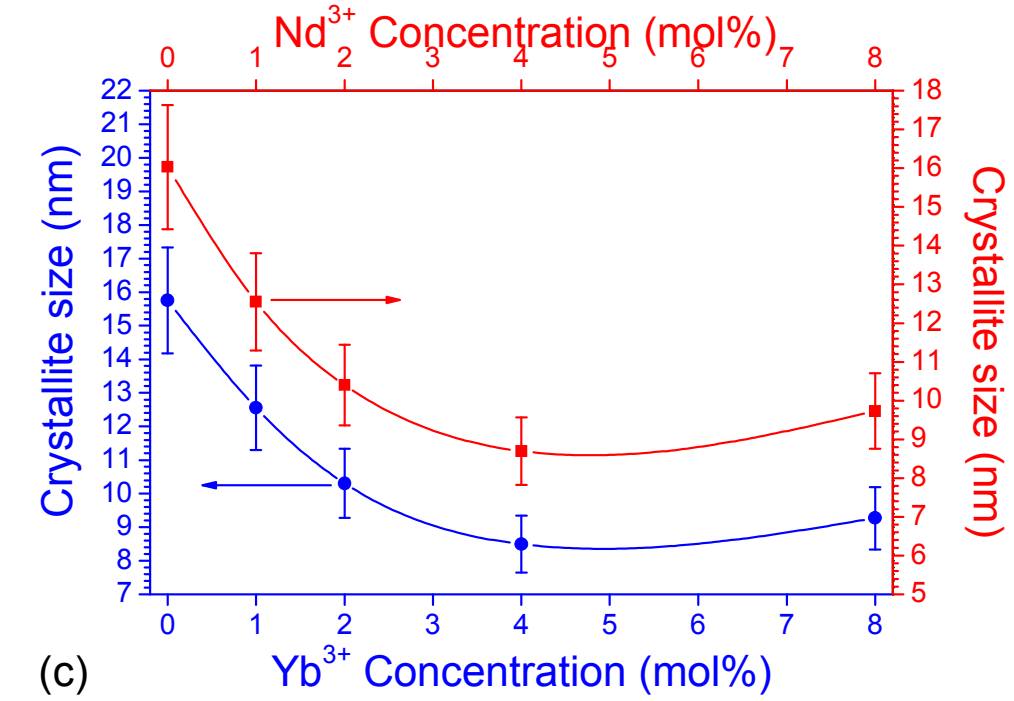
Nd3+ Concentration (mol%)
Crystallite size (nm)
Crystallite size (nm)
Yb3+ Concentration (mol%)
(c)

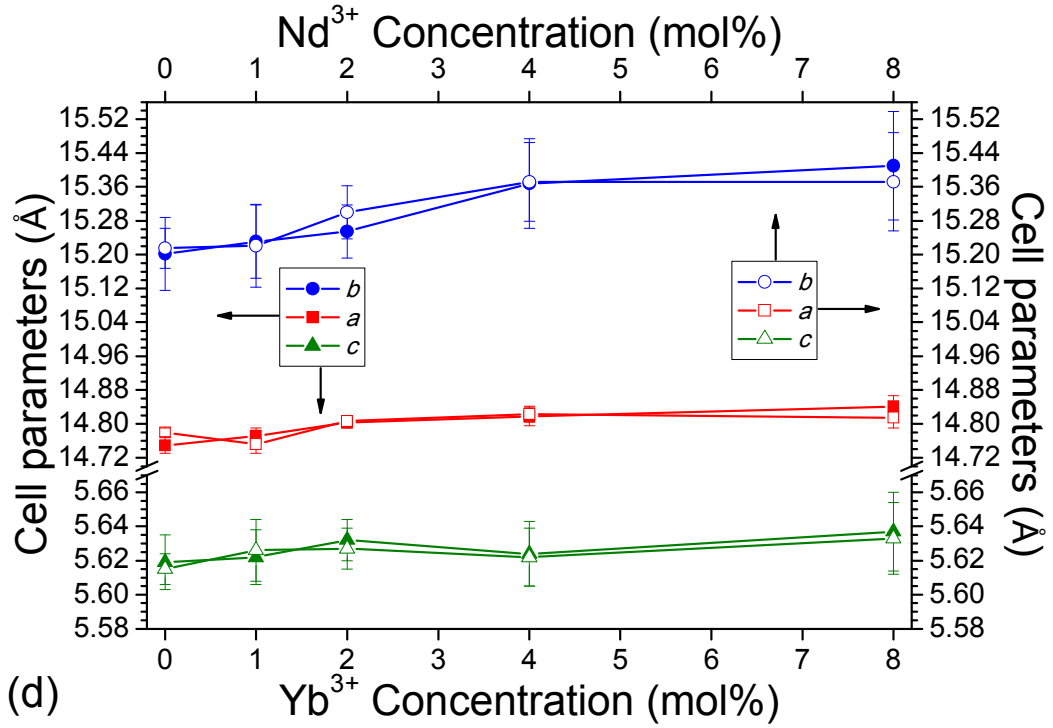
Nd3+ Concentration (mol%)
Cell parameters (Å)
Cell parameters (Å)
b
a
c
b
a
c
Yb3+ Concentration (mol%)
(d)

Figure 1.

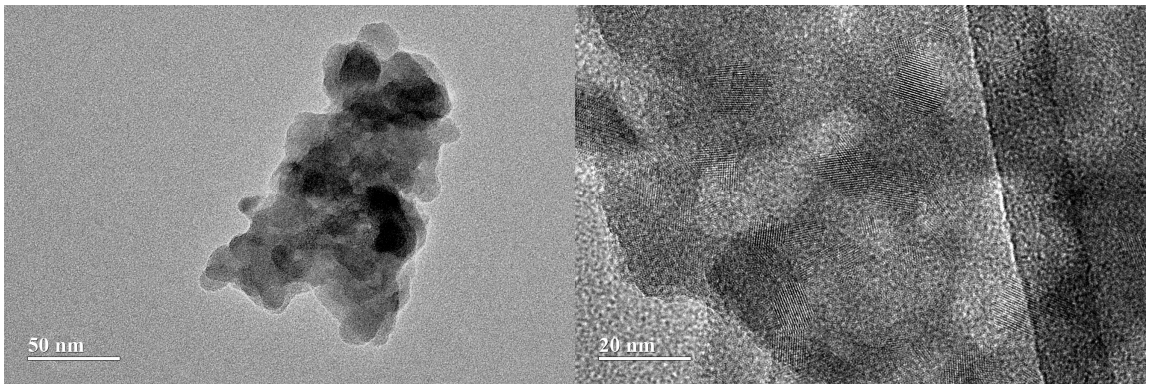

(a) (b)

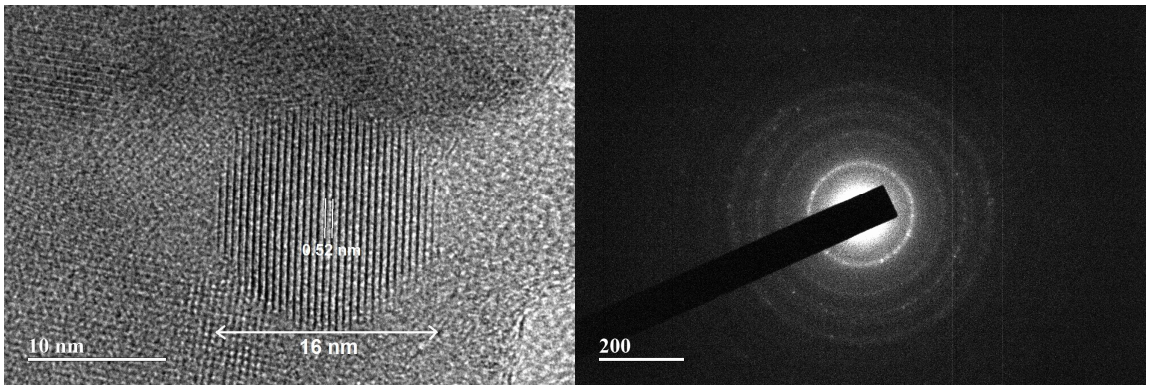

(c) (d)

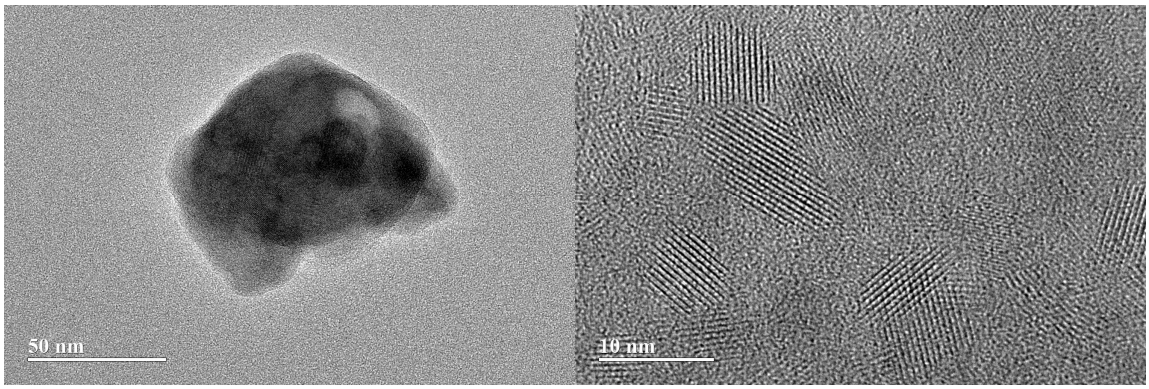

(e) (f)

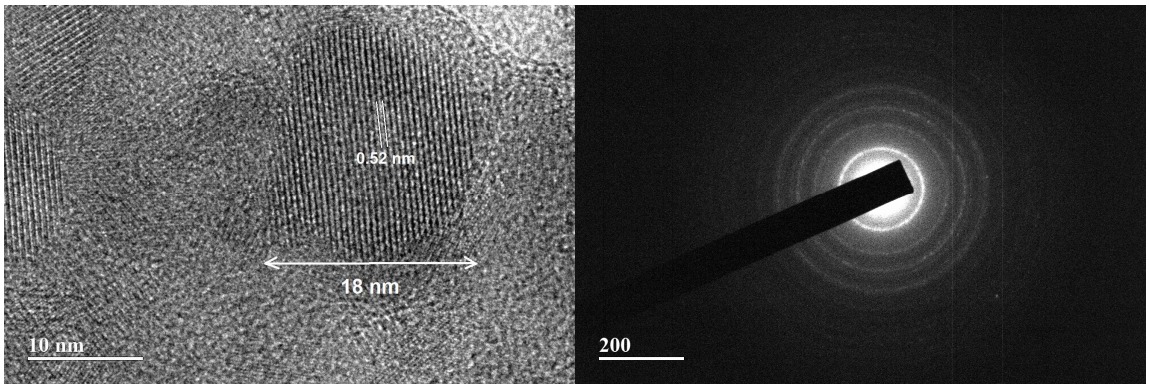

(g) (h)

Figure 2.

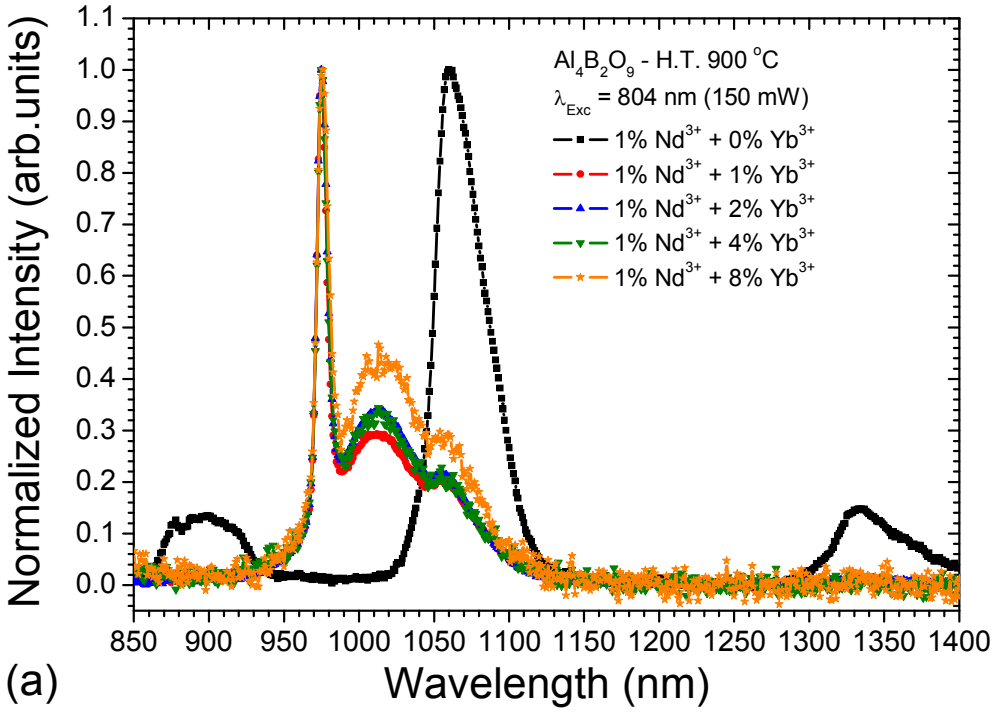
Al4B2O9 - H.T. 900 °C
λExc = 804 nm (150 mW)
1% Nd3+ + 0% Yb3+
1% Nd3+ + 1% Yb3+
1% Nd3+ + 2% Yb3+
1% Nd3+ + 4% Yb3+
1% Nd3+ + 8% Yb3+
Normalized Intensity (arb.units)
Wavelength (nm)

(a)

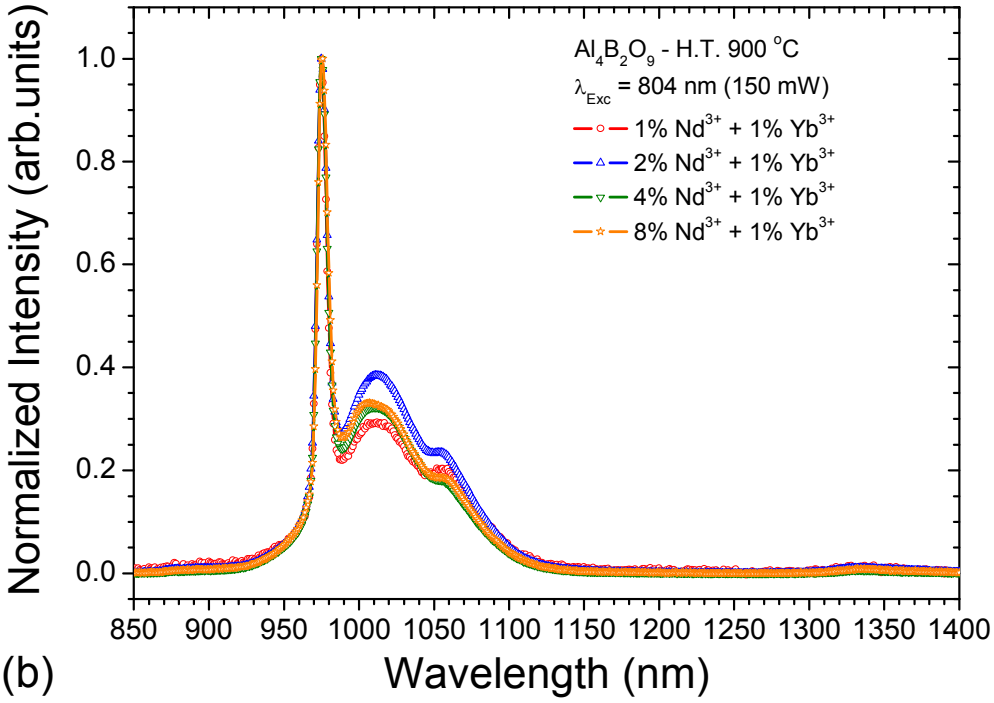
Al4B2O9 - H.T. 900 °C
λExc = 804 nm (150 mW)
1% Nd3+ + 1% Yb3+
2% Nd3+ + 1% Yb3+
4% Nd3+ + 1% Yb3+
8% Nd3+ + 1% Yb3+
Normalized Intensity (arb.units)
Wavelength (nm)

(b)

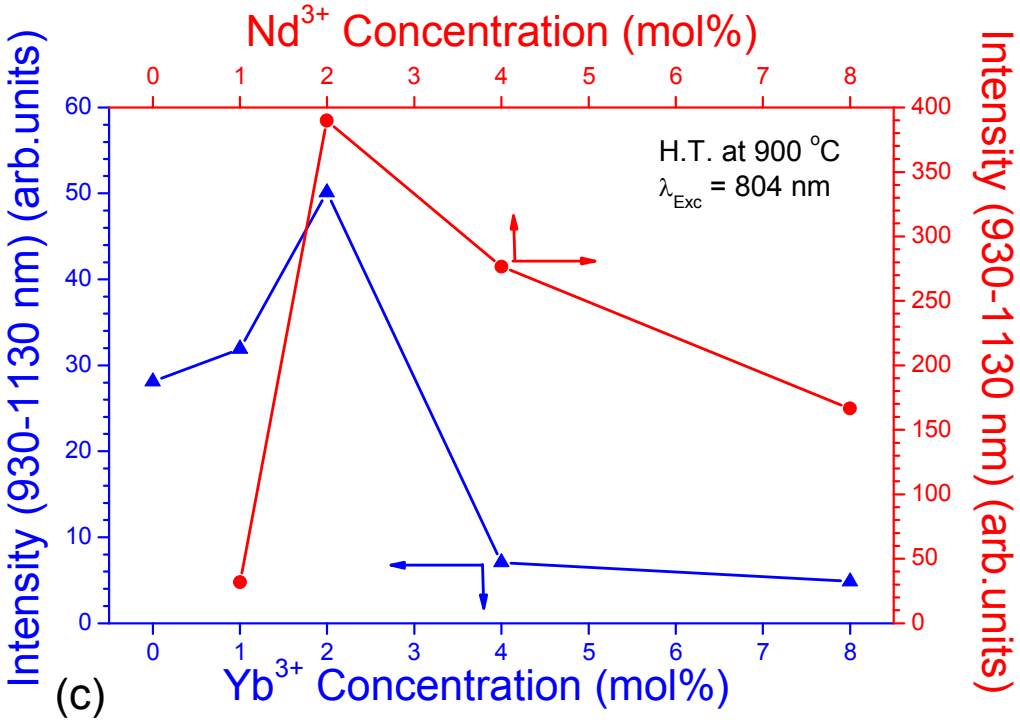
Nd3+ Concentration (mol%)
Yb3+ Concentration (mol%)
Intensity (930-1130 nm) (arb.units)
Intensity (930-1130 nm) (arb.units)
H.T. at 900 °C
λExc = 804 nm
(c)

Figure 3.

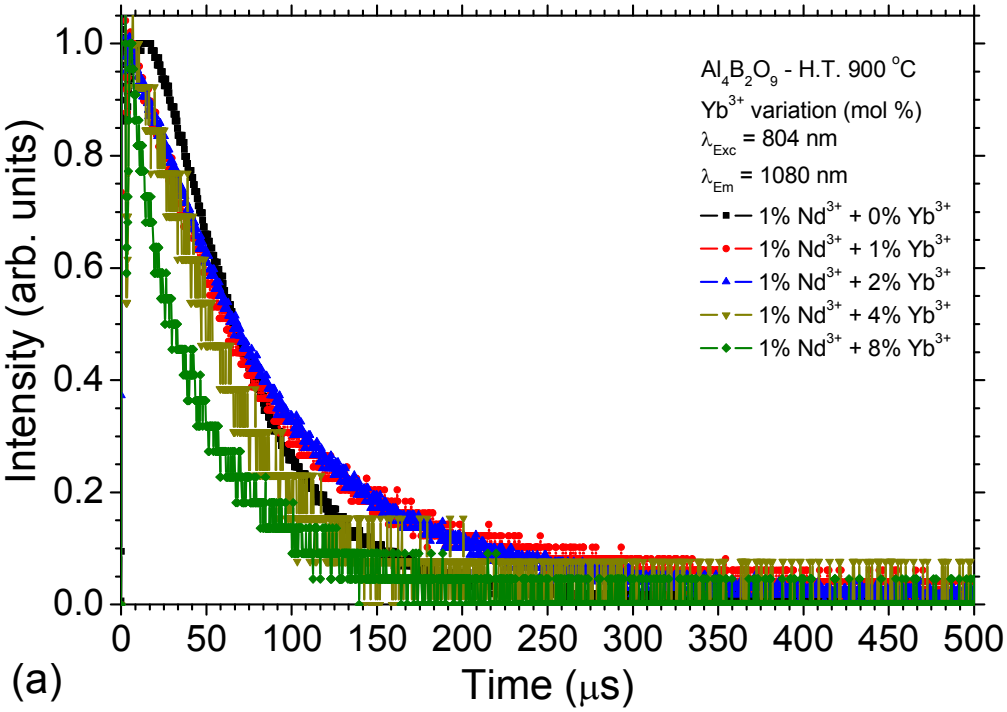
Al4B2O9 - H.T. 900 °C
Yb3+ variation (mol %)
λExc = 804 nm
λEm = 1080 nm
1% Nd3+ + 0% Yb3+
1% Nd3+ + 1% Yb3+
1% Nd3+ + 2% Yb3+
1% Nd3+ + 4% Yb3+
1% Nd3+ + 8% Yb3+
Intensity (arb. units)
Time (μs)
(a)

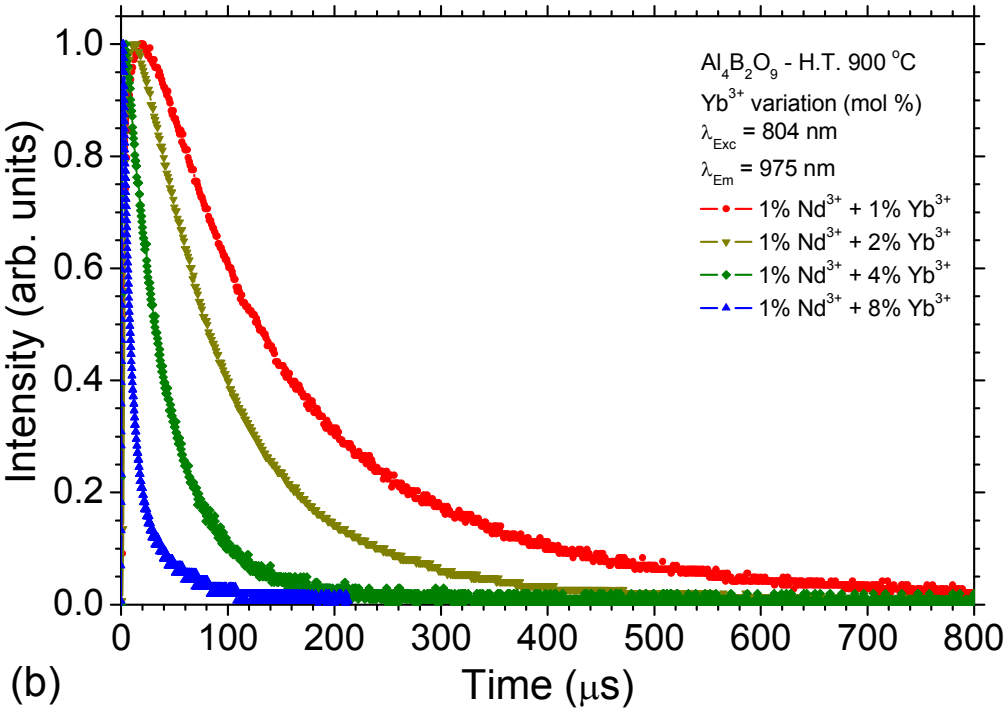
Al4B2O9 - H.T. 900 °C
Yb3+ variation (mol %)
λExc = 804 nm
λEm = 975 nm
1% Nd3+ + 1% Yb3+
1% Nd3+ + 2% Yb3+
1% Nd3+ + 4% Yb3+
1% Nd3+ + 8% Yb3+
Intensity (arb. units)
Time (μs)
(b)

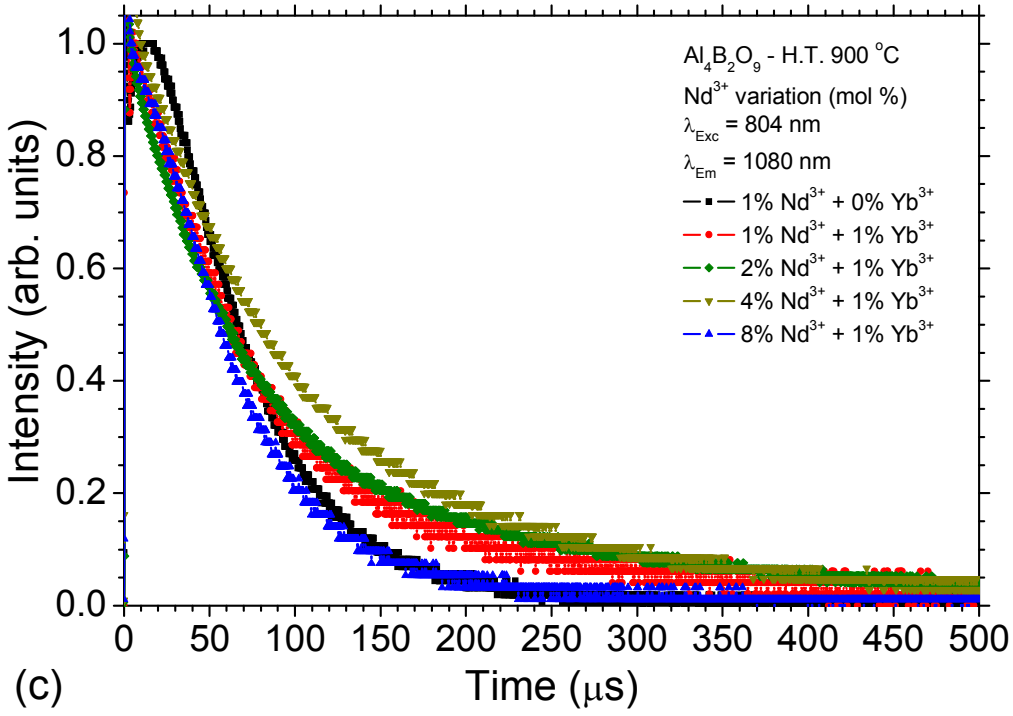
$Al_4B_2O_9$ - H.T. 900 °C
Nd^{3+} variation (mol %)
λ_{Exc} = 804 nm
λ_{Em} = 1080 nm
1% Nd^{3+} + 0% Yb^{3+}
1% Nd^{3+} + 1% Yb^{3+}
2% Nd^{3+} + 1% Yb^{3+}
4% Nd^{3+} + 1% Yb^{3+}
8% Nd^{3+} + 1% Yb^{3+}
Intensity (arb. units)
Time (μs)
(c)

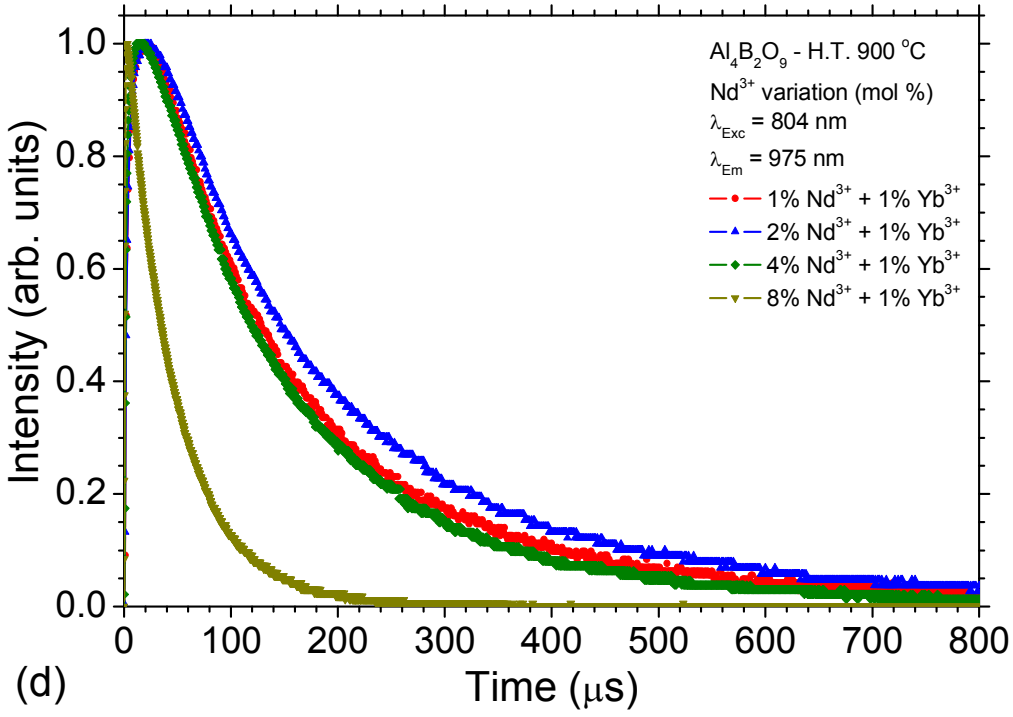
$Al_4B_2O_9$ - H.T. 900 °C
Nd^{3+} variation (mol %)
λ_{Exc} = 804 nm
λ_{Em} = 975 nm
1% Nd^{3+} + 1% Yb^{3+}
2% Nd^{3+} + 1% Yb^{3+}
4% Nd^{3+} + 1% Yb^{3+}
8% Nd^{3+} + 1% Yb^{3+}
Intensity (arb. units)
Time (μs)
(d)

Figure 4.

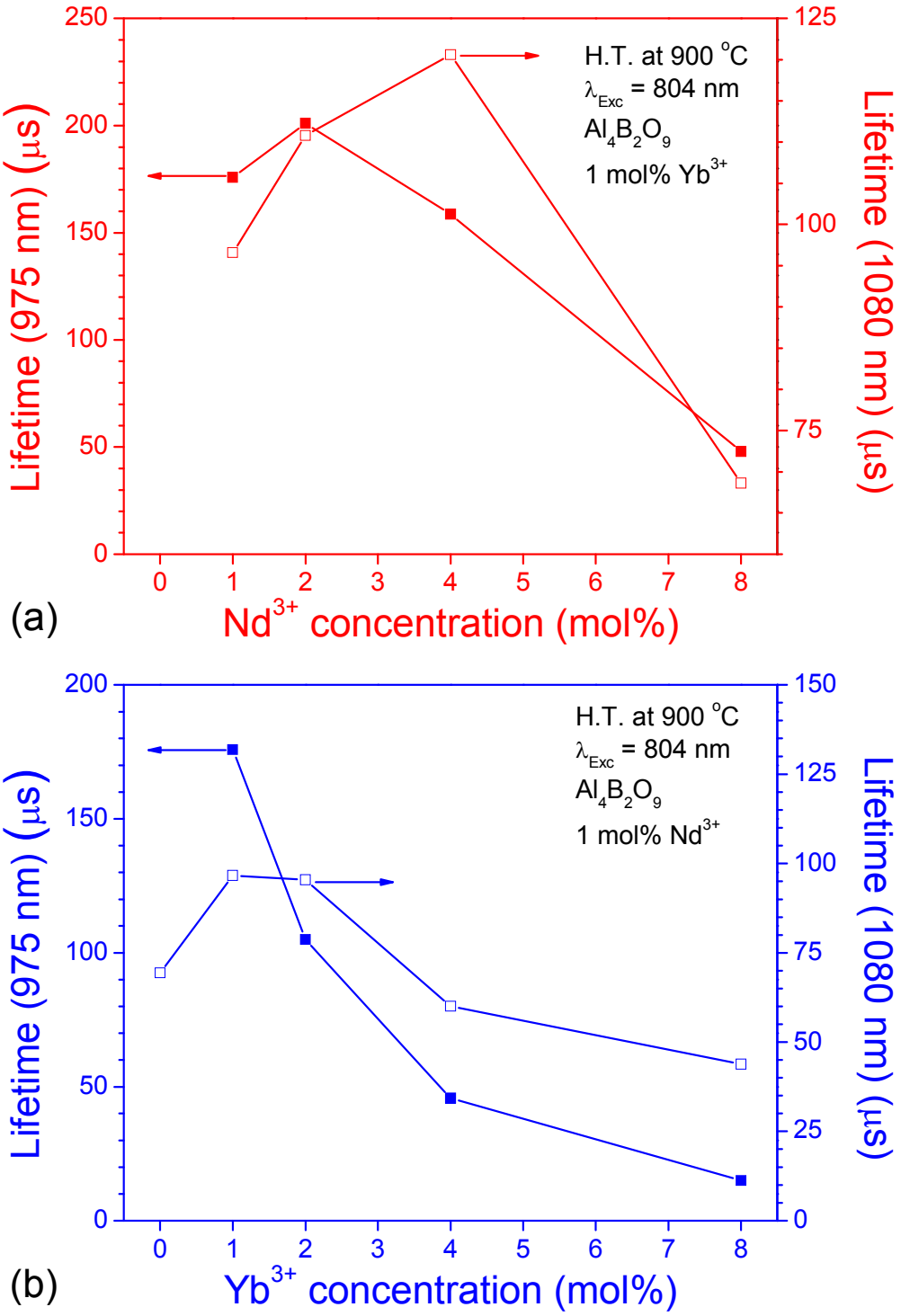
H.T. at 900 °C
λExc = 804 nm
Al4B2O9
1 mol% Yb3+
Lifetime (975 nm) (μs)
Lifetime (1080 nm) (μs)
Nd3+ concentration (mol%)
(a)
H.T. at 900 °C
λExc = 804 nm
Al4B2O9
1 mol% Nd3+
Lifetime (975 nm) (μs)
Lifetime (1080 nm) (μs)
Yb3+ concentration (mol%)
(b)

Figure 5.

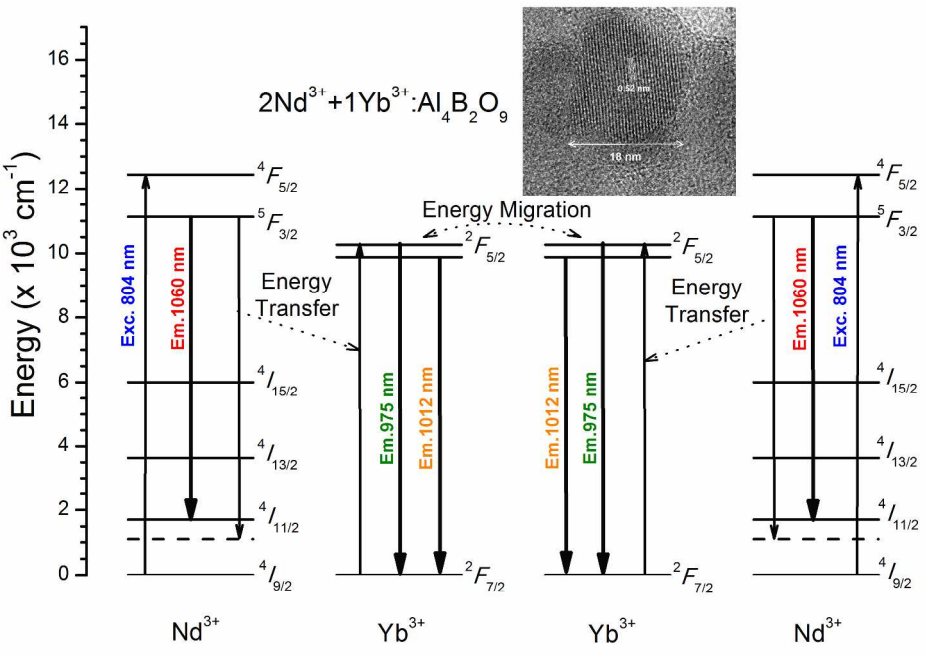

289x202mm (300 x 300 DPI)